arXiv:1302.5099v1 [cond-mat.str-el] 20 Feb 2013

# Frustration-Induced Magnetostructural Inhomogeneity in the Triangular Antiferromagnet $\alpha$-NaMnO$_2$

A. Zorko,[1,2,*] O. Adamopoulos,[3,4] M. Komelj,[1] D. Arčon,[1,5] and A. Lappas[3,†]
[1] *Jožef Stefan Institute, Jamova c. 39, 1000 Ljubljana, Slovenia*
[2] *EN–FIST Centre of Excellence, Dunajska c. 156, SI-1000 Ljubljana, Slovenia*
[3] *Institute of Electronic Structure and Laser, Foundation for Research and Technology – Hellas, Vassilika Vouton, 71110 Heraklion, Greece*
[4] *Department of Chemistry, University of Crete, Voutes, 71003 Heraklion, Greece*
[5] *Faculty of Mathematics and Physics, University of Ljubljana, Jadranska c. 19, 1000 Ljubljana, Slovenia*
(Dated: February 21, 2013)

We show that the triangular-lattice antiferromagnet $\alpha$-NaMnO$_2$ is endowed with a complex magnetostructurally inhomogeneous ground state, a result of intertwined spin and lattice degrees of freedom. Synchrotron X-ray diffraction, nuclear magnetic resonance and muon spin relaxation unveil that the magnetically frustrated monoclinic phase is disrupted by nanoscale regions of a triclinic structure. The magnetic order in the latter is uncorrelated with the monoclinic matrix, where bulk Néel order is initiated by the local-scale inhomogeneity. The phase separation is endorsed by frustration leading to quasi-elastic magnetic excitations that couple to competing structural phases.

PACS numbers: 75.80.+q, 76.60.-k, 76.75.+i, 64.75.-g

Complexity of phases is a common theme in systems with simultaneously active degrees of freedom – spin, charge, orbital, and/or phonon [7]. Owing to strong electronic correlations, nanometer-scale inhomogeneities, like stripes and checkerboard charge ordering in cuprates [2–4], as well as many other striking inhomogeneous states of manganites [5, 6], cobaltates [7], nickelates [8, 9], and iron pnictides [10, 11], can emerge even when Hamiltonians do not brake translational symmetry [7, 12]. In these systems inhomogeneity stems from the charge degrees of freedom and usually appears due to quenched disorder – random deviations from perfect system uniformity – that can dramatically alter the properties of materials entailing competing interactions [7]. In localized-spin systems, on the other hand, inhomogeneous phases are rare [13, 14] and still poorly understood, although they have been predicted to appear already in the clean limit of uniformly frustrated magnets [15, 16]. Geometrical frustration of a spin lattice [17, 18] is known for provoking novel fundamental phenomena in magnetism, like exotic disordered ground states [18, 19] and fractional spin excitations [19, 20]. Moreover, its involvement in structural instabilities has also been well documented, e.g., in relaxor ferroelectrics [21] and multiferroics [22]. Therefore, ground-state degeneracy of geometrically frustrated magnets, in alliance with the magnetoelastic coupling, could make the energetic cost of spatial fluctuations low, rendering these systems "electronically soft" [23] and thus prone to forming inhomogeneous states.

The layered $\alpha$-NaMnO$_2$ compound is intriguing in this respect, because of its atypical low-temperature magnetic state. It represents a spatially anisotropic triangular lattice of $S = 2$ (Mn$^{3+}$) spins with dominant intrachain ($J_1 = 65$ K) and frustrated interchain ($J_2 = 29$ K) antiferromagnetic exchange interactions [2] in the $ab$ crystallographic plane (Fig. 1). Both, sharp magnetic reflections and diffuse scattering were simultaneously observed in neutron powder diffraction (NPD), even far below the Néel temperature $T_N = 45$ K [1]. The coexistence of long-range magnetic order and short-range spin correlations indicates a magnetically inhomogeneous ground state. In addition, large and highly anisotropic microstrains in the crystal structure above $T_N$ suggest structural inhomogeneities. This is a likely precursor to the structural phase transition from a monoclinic to a triclinic symmetry, which was reported to occur concurrently with the magnetic transition due to magnetoelastic coupling [1]. Whether structural inhomogeneities remain present below $T_N$ and if they pertain to a possible magnetic phase separation are major unresolved issues.

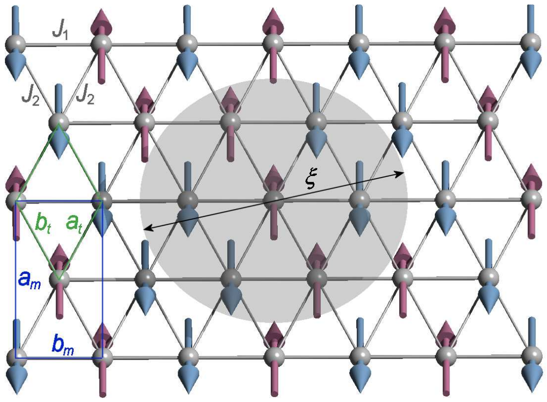

FIG. 1: Anisotropic triangular lattice of $S = 2$ (Mn$^{3+}$) spins in $\alpha$-NaMnO$_2$ with exchange interactions $J_1$, $J_2$ in the $ab$ crystallographic plane of the monoclinic ($m$) and the triclinic ($t$) cell settings. Long-range antiferromagnetic order [$\mathbf{k}_m = (\frac{1}{2}, \frac{1}{2}, 0)$] is interrupted by the shaded nano-sized magnetic-defect region, characterized by a correlation length $\xi$.

In this Letter, we combine synchrotron X-ray powder diffraction (XRD) with local-probe nuclear magnetic resonance (NMR) and muon spin relaxation ($\mu$SR) techniques, which provide insight to a unique magnetostructurally inhomogeneous ground state of $\alpha$-NaMnO$_2$. Its spatial complexity stems from simultaneously active spin and lattice degrees of freedom. We show that the relief of frustration by a lattice-distorting procedure, likely triggered by infinitesimal quenched disorder below $T_N$, is endorsed by quasi-elastic magnetic excitations and occurs with the spontaneous emergence of competing magnetic states on nanoscopic level.

We have performed a thorough structural investigation of $\alpha$-NaMnO$_2$, employing high-resolution synchrotron powder XRD (ID31 beam-line at the ESRF; $\lambda = 0.39986$ Å, $T = 5-300$ K) to gain insight on the large strain fields detected in the early NPD study [1]. The XRD confirms the single-phase nature of $\alpha$-NaMnO$_2$. At room temperature it crystallizes in the monoclinic structure [$C2/m$; $a = 5.67075(5)$ Å, $b = 2.85896(2)$ Å, $c = 5.80109(6)$ Å, $\beta = 113.1537(4)°$; Fig. 2(a)]. Rietveld refinements with the FULLPROF suite [26] show that, upon cooling, $hkl$-dependent anisotropic broadening of the Bragg reflections needs to be taken into account. We have utilized the Stephens's formalism [4] of anisotropic strain broadening ($S_{hkl}$) and found that the $S_{040}$ parameter is the largest and increases the most down to $T_N$ [Fig. 2(b)]. This suggests that the distribution of the $ac$-interplane distances is the broadest and highly affected when approaching $T_N$ from above, while the $ab$ ($S_{004}$) and $bc$ ($S_{400}$) interplane-distance distributions are much smaller and less temperature dependent. Qualitatively, the $S_{040}$ strains in the monoclinic structure may originate from minute shifts of the Mn-Mn spin-chains along the $b_m$ axis (see Fig. 1 and Ref. 28), a lattice distortion which can effectively lead to the triclinic structure ($P\bar{1}$) at $T < T_N$ [1]. This behavior implies that the system develops a precursor state, before the magnetoelastic effects lift the degeneracy of its ground state.

In contrast to the isostructural CuMnO$_2$ [5, 6], the high-resolution synchrotron XRD patterns of $\alpha$-NaMnO$_2$ below $T_N$ do not show any resolvable peak-splitting that would unambiguously confirm a bulk phase transformation to the lower-symmetry triclinic phase. Surprisingly, Rietveld refinements at $T < T_N$ on the highly parameterized, strained triclinic ($t$) phase produce a quality of fit which is statistically poorer compared to the model based on the strained monoclinic ($m$) phase, $\chi^2_t \approx 1.4\chi^2_m$ [28]. Furthermore, a close inspection of the Rietveld fitted patterns for the latter recognizes anisotropically broadened profiles, where the calculated pattern systematically misses intensity from the low- and high-angle tails of certain Bragg reflections [Fig. 2(c)]. It is worth noting that presence of defects [31], chemical or structural inhomogeneities [32] may be the reason for the development of short-scale regions, which can give-rise to unusually broadened profiles, like those of $\alpha$-NaMnO$_2$. A way of simulating such a behavior is by a two-phase (2$p$) Rietveld model accounting for a nanoscale mixture of phases. Significantly improved quality of fit [Fig. 2(d)], $\chi^2_{2p} \approx 0.35\chi^2_m$, is obtained with a spatially inhomogeneous model assuming coexistence of the monoclinic and the triclinic phases [28]. The latter has been found to attain a volume fraction of $\sim$35(1)% at 30 K, which marginally evolves down to 5 K. The majority monoclinic phase retains some strain, but this is severely relieved below $T_N$ [Fig. 2(b)] where the triclinic phase, with inequivalent interchain Mn-Mn distances [28], coexists with the former. Randomly distributed nanoscale inhomogeneities, pertaining to the minority phase ($P\bar{1}$) that is grown at the expense of the majority one ($C2/m$), may severely modify the macroscopic electronic response (*vide infra*) of the bulk compound. This renders it an intriguing subject for local-probe investigations.

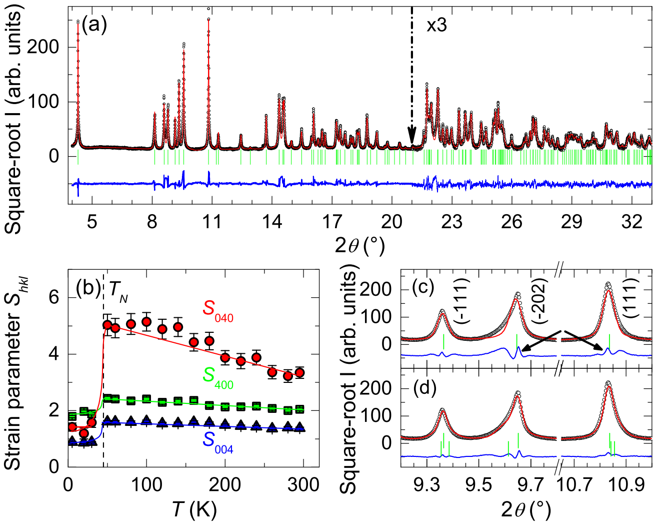

FIG. 2: (a) Observed (circles), calculated (full curve) and difference synchrotron XRD profiles of $\alpha$-NaMnO$_2$ at 295 K, after Rietveld refinement in the monoclinic symmetry ($C2/m$); predicted reflections are marked by vertical ticks. At $2\theta > 21°$ all pattern intensities were multiplied by 3 to increase clarity. (b) The temperature evolution of the anisotropic strain broadening parameters $S_{hkl}$ (lines are a guide to the eye). Detail of the 30 K profile after Rietveld fits with (c) a single strained monoclinic phase (important deviations in the difference plot are marked by arrows) and (d) coexisting strained monoclinic and unstrained triclinic phases.

In order to validate the apparent phase separation and associated local inhomogeneities in $\alpha$-NaMnO$_2$, we employed $^{23}$Na ($I = 3/2$) NMR [28], locally probing electronic (charge and magnetic) environment of the $^{23}$Na nuclei. A transferred hyperfine coupling $\underline{A}_{jk}$ of the nuclear spin $I_j$ with electronic spins $S_k$ on nearby Mn$^{3+}$ sites, $\mathcal{H}^{\mathrm{hf}}_j = \mathbf{I}_j \cdot \sum_k \underline{A}_{jk} \cdot \mathbf{S}_k = \hbar\gamma \mathbf{I}_j \cdot \underline{\delta} \cdot \mathbf{B}_0$ ($\hbar$ is the reduced Planck constant and $\gamma = 70.8$ MHz/T the $^{23}$Na gyromagnetic ratio), is responsible [28] for a sizable isotropic shift

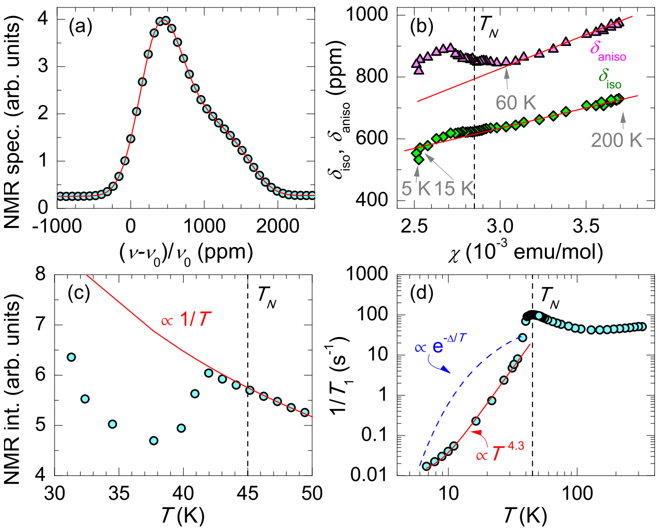

FIG. 3: (a) The central $(-\frac{1}{2} \leftrightarrow \frac{1}{2})$ line of the $^{23}$Na NMR spectrum in $\alpha$-NaMnO$_2$ at 300 K and 8.9 T. The solid line corresponds to the fitting, explained in the text. (b) Scaling of the isotropic $\delta_{\rm iso}$ (line shift) and anisotropic $\delta_{\rm aniso}$ (line width) hyperfine coupling constants with bulk susceptibility $\chi$ at 5 T. Solid lines are linear fits of the high-temperature data. (c) Partial wipe-out of the NMR signal (corrected for spin-spin relaxation) below $T_N$. (d) The $^{23}$Na spin-lattice relaxation rate exhibiting power-law dependence below $T_N$.

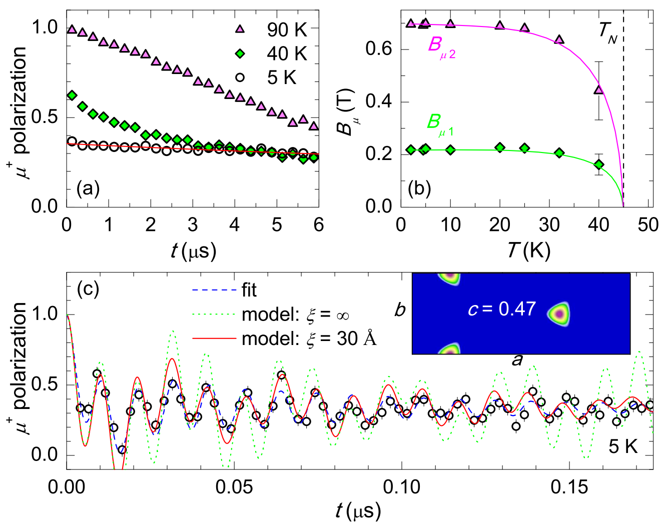

FIG. 4: (a) The decay of $\mu^+$ polarization above and below $T_N = 45$ K. The solid line corresponds to exponential decay. (b) The temperature evolution of the local magnetic field at muon sites (lines are a guide to the eye). (c) Experimental oscillations of $\mu^+$ polarization in the ordered state (circles). The lines show the fitting with two damped cosine contributions and modeling with nanoscopic inhomogeneities, as explained in the text. Inset: contour of the electrostatic potential in the $ab$ plane with highlighted global minima for the $P_1$ site.

[$\delta_{\rm iso} = 707(10)$ ppm at 300 K] and anisotropic broadening [$\delta_{\rm aniso} = 950(10)$ ppm] of the central $(-\frac{1}{2} \leftrightarrow \frac{1}{2})$ nuclear transition [Fig. 3(a)]. Our calculations [28] show that $\delta_{\rm aniso}$ corresponds to local dipolar fields while the finite $\delta_{\rm iso}$ proves that the inter-layer exchange effectively runs through the Na$^+$ sites.

The $\delta_{\rm iso}$ and $\delta_{\rm aniso}$ are determined by the average of a static local-field distribution at the $^{23}$Na site and its width, respectively. Therefore, they are both expected to scale with magnetic susceptibility $\chi$. This should remain the case even below $T_N$, since on the highly symmetric $^{23}$Na position (structural center of inversion) the local fields from antiferromagnetically ordered Mn$^{3+}$ moments at sites $\pm\mathbf{r}$ [1] effectively cancel out. Experimentally, we observe significant deviations form the linear scaling, particularly pronounced for $\delta_{\rm aniso}$ [Fig. 3(b)], which set in already at $\sim$ 60 K, i.e., far above $T_N = 45$ K. Since the $^{23}$Na quadrupolar-broadening effects are small [28] the deviations above $T_N$ signal an onset of short-range spin correlations. On the other hand, the apparent non-linearity $\delta_{\rm aniso} \not\propto \chi$ below $T_N$ discloses a more complicated magnetic order than initially proposed [1]. We stress that $\delta_{\rm aniso}$ does not exhibit an order-parameter dependence below $T_N$, hence, it cannot be explained by a small additional spin component that would break the symmetry at the $^{23}$Na sites. Quite importantly, we also find that close to $T_N$ the NMR intensity of the central line that would normally scale with $1/T$ due to the Boltzmann population factor, suddenly drops by $\sim$ 30% [Fig. 3(c)]. NMR thus clearly discloses a magnetic phase separation below $T_N$, where the remaining NMR component characterized by a zero static local magnetic field is accompanied by an unobservable component.

In order to expose the microscopic nature of the magnetic phase separation below $T_N$, we finally resort to $\mu$SR. This technique is extremely sensitive to local magnetic fields $B_\mu$, and directly measures their distribution in an ordered state through the relaxation function $P(t)$ of the muon polarization [9]. Zero-field (ZF) $\mu$SR experiments were performed on the General Purpose Surface-Muon Instrument (GPS) at the Paul Scherrer Institute, Switzerland. The phase transition at $T_N$ is clearly visible in reduced muon polarization below $T_N$ [Fig. 4(a)]. In a static local field $B_\mu$ such decrease results from averaging out fast oscillations in the relaxation function [9] $P_{\rm pwd}(t) = \frac{1}{3} + \frac{2}{3}\cos(\gamma_\mu B_\mu t)$ of a powder sample. We stress that below $T_N$ the polarization drops to 1/3, which is a clear indication that the bulk of the sample has undergone a transition into the ordered state. Oscillations in $P(t)$ below $T_N$ are evident at early times [Fig. 4(c)]. They reveal that two inequivalent muon stopping sites exist, as the polarization can be nicely fitted to the two-component model $P(t) = \sum_{j=1}^{2} f_j \left[\frac{1}{3}{\rm e}^{-\lambda_l t} + \frac{2}{3}\cos(\gamma_\mu B_{\mu,j}){\rm e}^{-\lambda_{t,j} t}\right]$. We find volume fractions $f_1$:$f_2$ = 60(5):40(5) that are temperature independent and internal fields $B_{\mu,j}$ that show an order-parameter-like temperature dependence [Fig. 4(b)].

We emphasize the large difference between the longitudinal $\lambda_l = 0.03(1)$ $\mu$s$^{-1}$ and the transverse $\lambda_{t1} = 82(5)$ $\mu$s$^{-1}$, $\lambda_{t2} = 12(1)$ $\mu$s$^{-1}$ relaxation rates at 5 K. The former is of dynamical origin, while the latter additionally encompasses a distribution of static local fields [9]. This distribution is obviously responsible for the fast damping of oscillations. In order to model it, the knowledge of muon stopping sites is required. Here, we rely on *ab-initio* calculation of the electrostatic potential of $\alpha$-NaMnO$_2$ [28], which predicts that the muons most likely stop at the $4i$ interstitial sites $P_1 = (0.18, 0, 0.47)$ and $P_2 = (0.45, 0, 0.75)$, the former corresponding to the global electrostatic-potential minimum [inset in Fig. 4(c)]. The calculated dipolar fields from antiferromagnetically ordered Mn$^{3+}$ moments on these sites match the experimentally determined fields $B_{\mu,j}$ [28].

The broad local-magnetic-field distributions at $P_1$ and $P_2$ provide a microscopic insight to the inhomogeneous magnetic state of $\alpha$-NaMnO$_2$. Most importantly, they can be related to the "parasitic" triclinic structural phase. We model the field distributions by introducing triclinic magnetic defects in the form of nano-sized islands with the magnetic order reversed at the interfaces with the monoclinic matrix (Fig. 1). We have considered these defect regions to be either one- (1D), two- (2D), or three-dimensional objects with a characteristic correlation length $\xi$, randomly positioned in the lattice so that a given fraction $p$ of Mn$^{3+}$ ions resides in them. Independent on their dimensionality, when $\xi = \infty$ (corresponding to stripe- and slab-shifts for 1D and 2D defects, respectively) we find narrow local-field distributions with only a few characteristic frequencies [28]. These are manifested in beating [Fig. 4(c)] rather than in damping of $P(t)$. On the other hand, for finite $\xi$ the field distributions become much broader [28] and, consequently, result in heavily damped $P(t)$. For $p = 0.35$, as derived from the above-presented structural analysis, we can reproduce the experimental damping of $P(t)$ at 5 K if $\xi = 30(5)$ Å [Fig. 4(c)]. Such dispersed finite-size defects are in conformity with the short-range ordered regions inferred by neutron diffraction [1]. Moreover, introduction of such defects also explains the sudden ~30% decrease of the NMR intensity below $T_N$. Namely, the defects locally break the inversion symmetry and lead to a two-peak local-field distribution at the $^{23}$Na sites [28]. The dominant peak remains positioned at $B_{\rm Na1} = 0$ and is modestly broadened, which may explain the increase of $\delta_{\rm aniso}$ below $\sim 60$ $K$ [Fig. 3(b)]. The second peak, on the other hand, is found at $B_{\rm Na2} = 0.26$ T, yielding the huge width of the corresponding NMR signal $B_{\rm Na2}/B_0 = 3\%$ that renders this component unobservable.

In order to shed light on the mechanism responsible for stabilizing the remarkable inhomogeneous ground state of $\alpha$-NaMnO$_2$, we last inspect its low-energy magnetic excitations. According to inelastic neutron scattering, a large gap ($\Delta_0 = 87$ K) due to single-ion anisotropy and 1D excitations dictate the ground state at zero field [3]. Since these measurements can easily miss a quasi-elastic part, we resort to the complementary $^{23}$Na spin-lattice relaxation study. Below $T_N$, the relaxation is governed by inelastic scattering of spin waves [35]. For gapped excitations the thermally-activated relaxation rate $1/T_1 \propto e^{-\Delta/T}$ is expected for $T \ll \Delta$, and the power-law dependence $1/T_1 \propto T^n$ for $T \gg \Delta$ [36]. Here $n \geq 2$ depends on the dimensionality of the spin-wave dispersion and the number of magnons assisting the relaxation process [35, 36]. The sharp suppression of $1/T_1$ at $T_N$ [Fig. 3(d)] proves that NMR indeed probes low-energy magnetic excitations. However, the expected exponential law with $\Delta = \Delta_0 - \mu B_0 = 53$ K ($\mu = 2.9\mu_B$ [1]) is not in consent with the data [Fig. 3(d)]. In clear contrast, the power law with $n = 4.3$ (and the additional low-temperature constant term $1/T_1^0 = 0.01$ s$^{-1}$ corresponding to residual relaxation) matches the experimental data very well. Deviations from this law are observed only in a critical region close to $T_N$. Thus, our NMR spin-lattice relaxation measurements clearly witness quasi-elastic magnetic excitations. These can be explained by sliding magnetic stripes along the $b_m$ axis, an effect that costs zero energy in the monoclinic setting due to the frustrated nature of the interchain exchange $J_2$. As the individual stripes can shift independently, the ensemble of such excitations becomes extended. In alliance with the magnetoelastic coupling, they provide a likely rationalization of the observed unique magnetostructural inhomogeneity in $\alpha$-NaMnO$_2$.

In summary, we have discovered a magnetostructurally inhomogeneous ground state in $\alpha$-NaMnO$_2$ that entails defect nanoscale regions of the triclinic phase, where magnetic order is altered with respect to the long-range ordered monoclinic phase. The Néel order in the latter is likely governed by interphase boundaries or structural defects which pin the spin arrangement in the otherwise frustrated triangular layer topology. The observed inhomogeneity is in sharp contrast to superconducting cuprates and iron pnictides, colossal-magnetoresistant manganites and the majority of other examples, where microscopic phase separation originates from charge degrees of freedom [2–7, 7–12]. Moreover, the existence of nanodomains in these systems depends on doping, while $\alpha$-NaMnO$_2$ resides in the clean limit. We associate its remarkable ground state to a fierce competition between the monoclinic and the triclinic structure, whose energies are indistinguishable according to *ab-initio* calculations [37]. The energy difference remains minimal when exchange interactions are considered [37, 38]. This near-degeneracy enables even infinitesimal quenched disorder to locally lift the inherent geometrical frustration of the triangular lattice in the monoclinic phase. Thus, we propose that the geometrical frustration can lead to inhomogeneities in the magnetoelastic channel, which represents an intriguing novelty among phase-separated states of highly correlated electron systems.

We are grateful to A. Abakumov for useful discussions, A. Amato for assistance with the $\mu$SR measurements and I. Margiolaki for help with the ID31, ESRF experiments. We acknowledge the financial support of the Slovenian Research Agency (Project No. J1-2118) and EU FP6 (Contract No. 011723-RICN). Access to the synchrotron radiation facilities at ESRF is gratefully acknowledged.

---

[*] Electronic address: andrej.zorko@ijs.si
[†] Electronic address: lappas@iesl.forth.gr

[1] E. Dagotto, Science **309**, 257 (2005).
[2] J. M. Tranquada, B. J. Sternlieb, J. D. Axe, Y. Nakamura, and S. Uchida, Nature **375**, 561 (1995).
[3] T. Hanaguri, C. Lupien, Y. Kohsaka, D.-H. Lee, and M. Azuma, Nature **430**, 1001 (2004).
[4] For a review see M. Vojta, Adv. Phys. **58**, 699 (2009).
[5] For a review see E. Dagotto, T. Hotta, and A. Moreo, Phys. Rep. **344**, 1 (2001).
[6] J. C. Loudon, N. D. Mathur, and P. A. Midgley, Nature **420**, 797 (2002).
[7] M. Roger, D. J. P. Morris, D. A. Tennant, M. J. Gutmann, and J. P. Goff, Nature **445**, 631 (2007).
[8] J. M. Tranquada, D. J. Buttrey, V. Sachan, and J. E. Lorenzo, Phys. Rev. Lett. **73**, 1003 (1994).
[9] E. Wawrzyńska, R. Coldea, E. M. Wheeler, I. I. Mazin, M. D. Johannes, T. Sörgel, M. Jansen, R. M. Ibberson, and P. G. Radaelli, Phys. Rev. Lett. **99**, 157204 (2007).
[10] J. T. Park *et al.*, Phys. Rev. Lett. **102**, 117006 (2009).
[11] G. Lang, H.-J. Grafe, D. Paar, F. Hammerath, K. Manthey, G. Behr, J. Werner, and B. Büchner, Phys. Rev. Lett. **104**, 097001 (2010).
[12] V. B. Shenoy, D. D. Sarma, and C. N. R. Rao, ChemPhysChem **7**, 2053 (2006).
[13] A. Zorko, P. Jeglič, A. Potočnik, D. Arčon, A. Balčytis, Z. Jagličić, X. Liu, A. L. Tchougréeff, and R. Dronskowski, Phys. Rev. Lett. **107**, 047208 (2011).
[14] S. Nakajima, T. Suzuki, Y. Ishii, K. Ohishi, I. Watanabe, T. Goto, A. Oosawa, N. Yoneyama, N. Kobayashi, F. L. Pratt, and T. Sasaki, J. Phys. Soc. Jpn. **81**, 065706 (2012).
[15] J. Schmalian and P. G. Wolynes, Phys. Rev. Lett. **85**, 836 (2000).
[16] Y. Mu and Y. G. Ma, J. Chem. Phys. **117**, 1686 (2002).
[17] G. Misguich and C. Lhuillier, *Frustrated Spin Systems*, edited by H. T. Diep (World-Scientific, Singapore, 2005).
[18] *Introduction to Frustrated Magnetism*, edited by C. Lacroix, P. Mendels, and F. Mila (Springer-Verlag, Berlin, 2011).
[19] L. Balents, Nature **464**, 199 (2010).
[20] T.-H. Han, J. S. Helton, S. Chu, D. G. Nocera, J. A. Rodriguez-Rivera, C. Bloholm, and Y. S. Lee Nature **492**, 406 (2012).
[21] J. Hemberger, P. Lunkenheimer, R. Fichtl, H.-A. Krug von Nidda, V. Tsurkan, and A. Loidl, Nature **434**, 364 (2005).
[22] S. W. Cheong and M. Mostovoy, Nat. Mater. **6**, 13 (2007).
[23] G. C. Milward, M. J. Calderón, and P. B. Littlewood, Nature **433**, 607 (2005).
[24] A. Zorko, S. El Shawish, D. Arčon, Z. Jagličić, A. Lappas, H. van Tol, and L. C. Brunel, Phys. Rev. B **77**, 024412 (2008).
[25] M. Giot, L. C. Chapon, J. Androulakis, M. A. Green, P. G. Radaelli, and A. Lappas, Phys. Rev. Lett. **99**, 247211 (2007).
[26] J. Rodríguez-Carvajal, Physica B **192**, 55 (1993).
[27] P. W. Stephens, J. Appl. Cryst. **32**, 281 (1999).
[28] See Supplemental Information material for details on the structural analysis of the ID31 synchrotron XRD data, the $^{23}$Na NMR measurements, the determination of the muon stopping sites, and the dipolar-field calculations.
[29] C. Vecchini, M. Poienar, F. Damay, O. Adamopoulos, A. Daoud-Aladine, A. Lappas, J. M. Perez-Mato, L. C. Chapon, and C. Martin, Phys. Rev. B **82**, 094404 (2010).
[30] M. Poienar, C. Vecchini, G. André, A. Daoud-Aladine, I. Margiolaki, A. Maignan, A. Lappas, L. Chapon, M. Hervieu, F. Damay, and C. Martin, Chem. Mater. **23**, 85 (2011).
[31] L. Croguennec, P. Deniard, R. Brec, and A. Lecerf, J. Mater. Chem. **7**, 511 (1997).
[32] A. Lappas, K. Prassides, F. N. Gygax, and A. Schenck, J. Phys.: Condens. Matter **12**, 3401 (2000).
[33] A. Yaouanc and P. Dalmas de Réotier *Muon Spin Rotation, Relaxation and Resonance* (Oxford University Press, Oxford, 2011).
[34] C. Stock, L. C. Chapon, O. Adamopoulos, A. Lappas, M. Giot, J. W. Taylor, M. A. Green, C. M. Brown, and P. G. Radaelli, Phys. Rev. Lett. **103**, 077202 (2009).
[35] T. Moriya, Prog. Theor. Phys. **16**, 23 (1956).
[36] F. Mila and T. M. Rice, Phys. Rev. B **40**, 11382 (1989).
[37] Z.W. Ouyang and B. Wang, Phys. Rev. B **82**, 064405 (2010).
[38] T. Jia, G. Zhang, X. Zhang, Y. Guo, Z. Zeng, and H. Q. Lin, J. Appl. Phys. **109**, 07E102 (2011).

# Supplementary information: Frustration-Induced Magnetostructural Inhomogeneity in the Triangular Antiferromagnet $\alpha$-NaMnO$_2$

A. Zorko,[1,2] O. Adamopoulos,[3,4] M. Komelj,[1] D. Arčon,[1,5] and A. Lappas[3]

[1] *Jožef Stefan Institute, Jamova c. 39, SI-1000 Ljubljana, Slovenia*
[2] *EN–FIST Centre of Excellence, Dunajska c. 156, SI-1000 Ljubljana, Slovenia*
[3] *Institute of Electronic Structure and Laser, Foundation for Research and Technology – Hellas, Vassilika Vouton, 71110 Heraklion, Greece*
[4] *Department of Chemistry, University of Crete, Voutes, 71003 Heraklion, Greece*
[5] *Faculty of Mathematics and Physics, University of Ljubljana, Jadranska c. 19, 1000 Ljubljana, Slovenia*

## Structural Considerations

High-resolution synchrotron XRD patterns were collected at the ID31 beam-line in the ESRF ($\lambda = 0.39986$ Å, $T = 5 - 300$ K), on the same high-quality polycrystalline samples that were used before [1–3]. At 300 K $\alpha$-NaMnO$_2$ crystallizes in the monoclinic structure [$C2/m$; Rietveld refinement R-factors not corrected for background, $R_p = 11.6\%$, $R_{\rm wp} = 15.8\%$, $R_{\rm exp} = 3.80\%$, $\chi^2 = 17.3$; see Fig. 2(a) of the main part], a variant of the prototype rhombohedral delafossite, due to the presence of Jahn-Teller active Mn$^{3+}$ cations. Upon cooling, this phase evolves by showing $hkl$-dependent anisotropic broadening, which in the Rietveld refinements was modeled by the Stephens's formalism ($S_{hkl}$) [4], including a pseudo-Voigt peak-shape function. We find that the $S_{040}$ parameter, measuring the covariance $\langle(\alpha_2 - \langle\alpha_2\rangle)^2\rangle$ of the distribution of the metric parameter $\alpha_2 = 1/b^{*2}$ [4], is the largest and increases the most between 300 K and $T_N$ [Fig. 2(b) of the main part]. The strain fields in the monoclinic structure can originate from minute shifts of the Mn spin-chains along the $b_m$ axis (Fig. 5).

Although the ID31 synchrotron experiment provides an increased angular resolution (nominal instrumental contribution to the FWHM is ~ 0.003° in $2\theta$) as compared to the previous NPD structural study (FWHM was ~ 0.3° in $2\theta$), the synchrotron XRD patterns of $\alpha$-NaMnO$_2$ below $T_N$ do not show any resolvable peak-splitting (Fig. 6), in contrast to the isostructural CuMnO$_2$ phase [5, 6]. In the latter compound such a feature signals a bulk phase transformation to the triclinic cell. Rietveld refinements at $T < T_N$ on the highly parameterized (as defined by the much larger number of generated reflections due to -1 Laue symmetry) strained $P\bar{1}$ phase produces a quality of fit [$R_p = 17.2\%$, $R_{\rm wp} = 22.4\%$, $R_{\rm exp} = 3.9\%$, $\chi^2 = 32.3$; Fig. 7(a)] which is poorer than that of the strained $C2/m$ phase [$R_p = 14.9\%$, $R_{\rm wp} = 18.9\%$, $R_{\rm exp} = 3.9\%$, $\chi^2 = 23.1$; Fig. 7(b)]. The $\alpha$-NaMnO$_2$ data at $T < T_N$ lack peak-splitting, however, a close inspection of the Rietveld fitted patterns in the monoclinic phase recognizes that the calculated profile systematically misses some intensity from different regions of the observed diffraction profile [Fig. 8(a)].

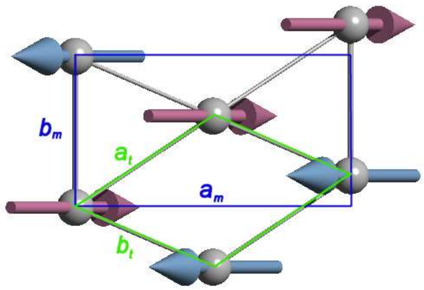

FIG. 5: Schematic of the lattice-distorting in $\alpha$-NaMnO$_2$ at the transition from the monoclinic ($m$) to the triclinic ($t$) phase. The Mn-Mn antiferromagnetic $S = 2$ chains shift along the $b_m$ axis. Arrows indicate the ordered magnetic moments.

Modeling such anisotropically broadened profiles may assume a nanoscale mixture of phases, where, in a sim-

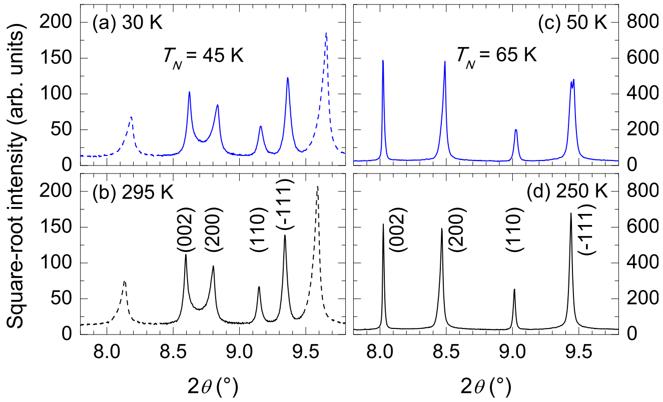

FIG. 6: Part of the synchrotron powder X-ray diffraction patterns from the ID31 beam-line at the ESRF ($\lambda = 0.39986$ Å) for (a, b) $\alpha$-NaMnO$_2$ and (c, d) the isomorphous CuMnO$_2$, above and below the transition to the Néel ordered state ($T_N$). The $hkl$-dependent anisotropic broadening of the Bragg peaks is evident in the former, whereas characteristic peak-splitting of certain families of Bragg reflections in CuMnO$_2$ signifies a bulk phase transformation from the monoclinic to the triclinic structure.

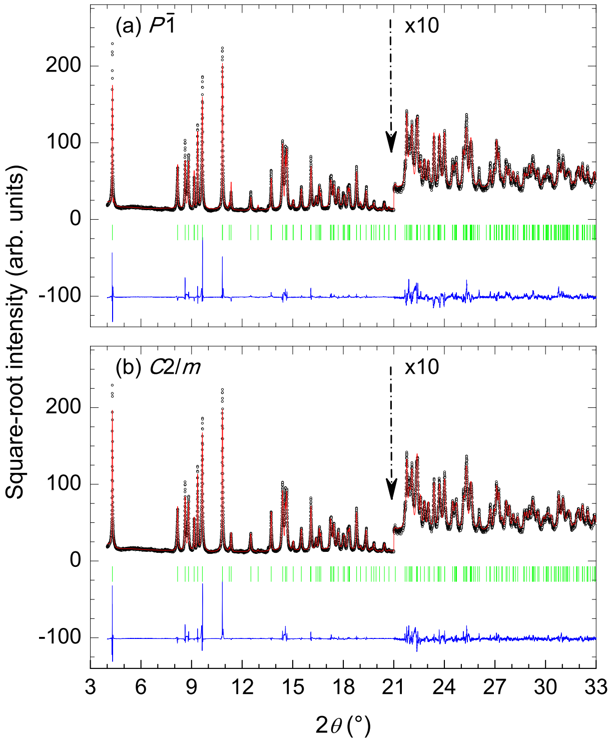

FIG. 7: Single-phase Rietveld refinement of $\alpha$-NaMnO$_2$ at 30 K, (a) in the triclinic cell setting ($a$ = 3.16371(6) Å, $b$ = 3.16127(8) Å, $c$ = 5.77519(6) Å, $\alpha$ = 110.340(2)°, $\beta$ = 110.316(1)°, $\gamma$ = 53.7094(8)° and (b) in the monoclinic cell setting, $a$ = 5.64258(7) Å, $b$ = 2.85725(3) Å, $c$ = 5.77284(9) Å, $\beta$ = 112.9123(7)°. Large deviations between observed and calculated profiles are depicted in the difference plot.

plified approach, a multi-phase Rietveld fit describes the data. Once the strained monoclinic and unstrained triclinic phases are allowed to coexist, a significantly improved quality of fit is attained ($R_p$ = 8.7%, $R_{\rm wp}$ = 11.3%, $R_{\rm exp}$ = 3.9%, $\chi^2$ = 8.2; Fig. 8(b), Fig. 9), yielding a "parasitic" triclinic phase with a volume fraction of $\sim$ 35(1)%, which is retained down to 5 K. Nanoscale structural inhomogeneities may unveil the presence of quenched disorder [7]. However, this cannot be well-resolved from the present powder diffraction data and requests high-resolution transmission electron microscopy, as exploited before for the non-stoichiometric CuMnO$_2$ phases [6]. The temperature evolution of the in-plane Mn-Mn separation indicates a lattice distortion procedure, which gives rise to the relief of strain and the inequality of the two interchain Mn-Mn distances below about $T_N$ [Fig. 10(a)]. The temperature evolution of the $\alpha$-NaMnO$_2$ unit-cell volume shows normal thermal contraction, whereas the coexisting triclinic phase holds half of the monoclinic cell volume [Fig. 10(b)].

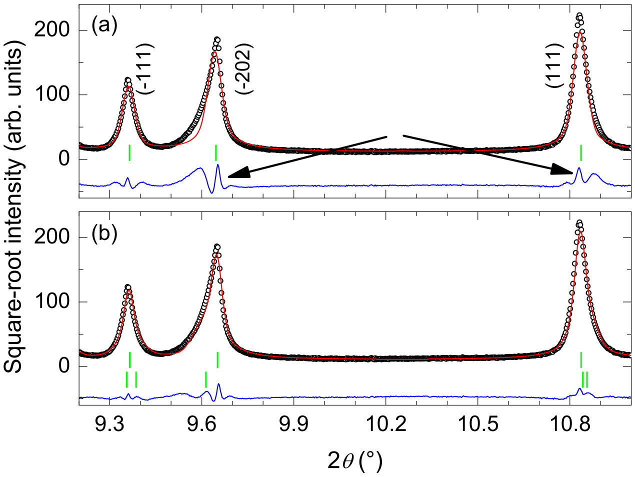

FIG. 8: A detail of the 30 K profile of $\alpha$-NaMnO$_2$ fitted by the Rietveld method on the basis of (a) a single-phase model entailing a strained monoclinic phase and (b) a two-phase model involving the coexistence of strained monoclinic and unstrained triclinic phases. Arrows mark important deviations in the difference plot due to inadequacies of the calculated profile of the single-phase model.

### $^{23}$Na **NMR experiments**

Frequency-swept $^{23}$Na ($I$ = 3/2) NMR spectra were measured on a home-built spectrometer in the fixed magnetic field $B_0$ = 8.9 T and obtained with a solid-

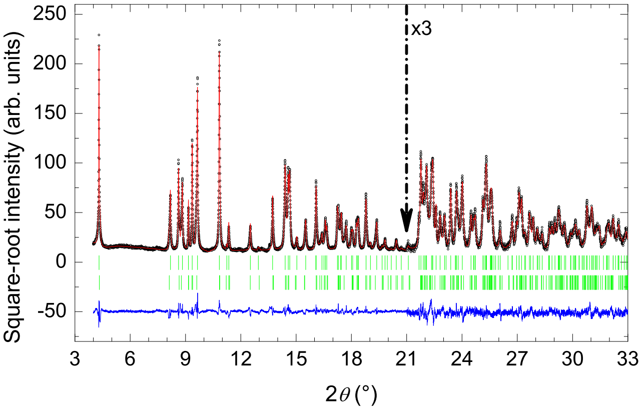

FIG. 9: Observed (circles), calculated (full curve) and difference synchrotron XRD profiles of $\alpha$-NaMnO$_2$ at 30 K, after Rietveld refinement with a two-phase model assuming coexistence of monoclinic ($C2/m$; $a$ = 5.63750(3) Å, $b$ = 2.85763(1) Å, $c$ = 5.77295(3) Å, $\beta$ = 112.8926(4)°) and triclinic ($P\bar{1}$; $a$ = 3.1814(2) Å, $b$ = 3.1751(2) Å, $c$ = 5.7589(2) Å, $\alpha$ = 110.429(3)°, $\beta$ = 110.589(4)°, $\gamma$ = 53.308(3)°) phases; predicted reflection positions are marked by the vertical ticks (top set : monoclinic and bottom set: triclinic space groups). At $2\theta > 21°$ all pattern intensities were multiplied by 3 to increase clarity.

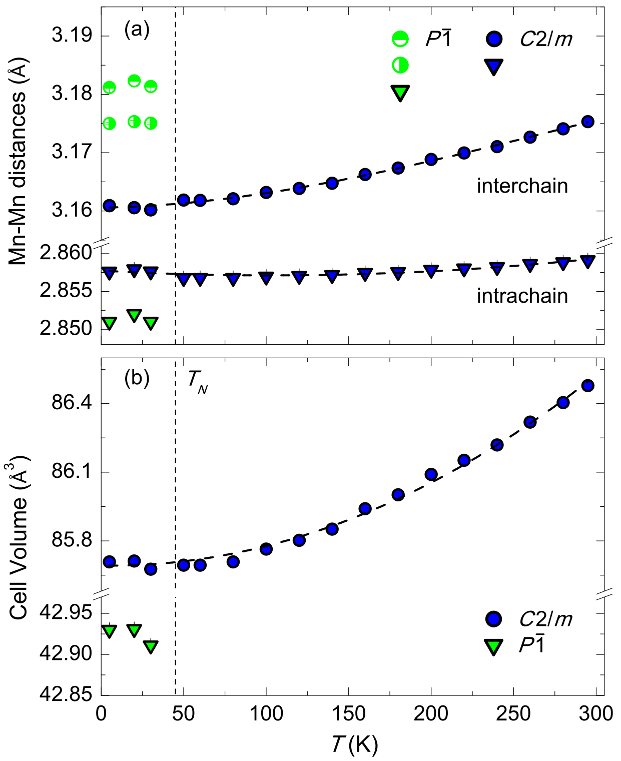

FIG. 10: (a) Temperature evolution of the inplane Mn-Mn distances in the two unit-cell settings, monoclinic ($C2/m$) and triclinic ($P\bar{1}$), as derived by the Rietveld refinements of the synchrotron XRD data. Below $T_N$ Rietveld fits were undertaken with the model assuming coexistence of strained monoclinic and unstrained triclinic phases. (b) The $T$-evolution of the monoclinic and triclinic unit cell volumes.

echo pulse sequence. The $\pi/2$ pulse length was 3.4 $\mu$s. Spin-lattice relaxation ($1/T_1$) measurements utilized an inversion-recovery sequence at the peak of the central ($-\frac{1}{2} \leftrightarrow \frac{1}{2}$) nuclear transition. The NMR line shift was measured relative to the reference Larmor frequency $\nu_0 = 100.5255$ MHz, corresponding to the NMR signal of a 0.1 M NaCl solution.

The $^{23}$Na spectrum recorded at 300 K is shown in Fig. 11. It consists of a sharp central line ($-1/2 \leftrightarrow 1/2$) and satellite transitions ($\pm1/2 \leftrightarrow \pm3/2$), broadened by a quadrupolar coupling in first order. The satellites and the central transition are strongly non-symmetric, implying that anisotropic magnetic coupling with Mn$^{3+}$ magnetic moments is large. The model Hamiltonian used for fitting the spectrum included the Zeeman part, the quadrupolar coupling of the nuclear quadrupolar moment with local electric-field gradients (EFG) and uniaxial anisotropic hyperfine coupling of the nuclear magnetic moments $I_j$ and Mn$^{3+}$ electronic moments, $\mathcal{H}^{\rm hf} = \hbar\gamma\sum_j \mathbf{I}_j\cdot\underline{\delta}\cdot\mathbf{B}_0$ ($\hbar$ is the reduced Planck constant, $\gamma = 70.8$ MHz/T). Isotropic powder averaging was performed. The obtained EFG asymmetry parameter is $\eta = 0.54(3)$ and the quadrupolar frequency is $\nu_Q = 1.51(5)$ MHz, which is a rather typical value for the $^{23}$Na nuclei. The isotropic part of the hyperfine magnetic coupling tensor $\underline{\delta}_{\rm iso}$, which is responsible for the shift of the central line from the reference frequency $\nu_0$, is $\delta_{\rm iso} = 707(10)$ ppm at 300 K. The anisotropic part responsible for the line shape of the central transition, has the principal eigenvalue $\delta_{\rm aniso} = 950(10)$ ppm at 300 K. The quadrupolar interaction leads to the second-order shift -20 ppm and the width 100 ppm of the central line, which is small compared to the effect of the hyperfine interaction. The typical chemical-shift range -60 – 10 ppm for $^{23}$Na is also negligible.

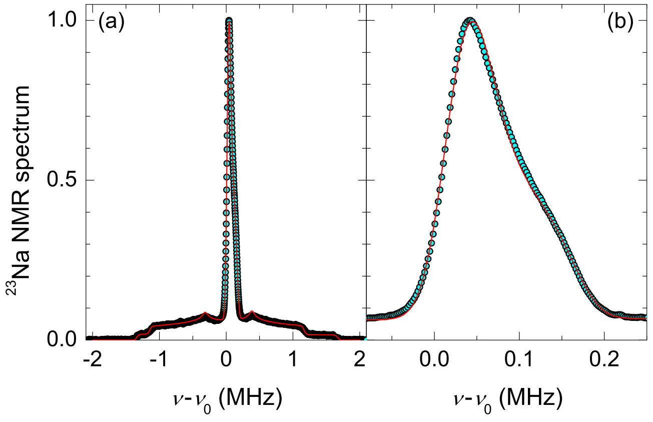

FIG. 11: (a) The $^{23}$Na NMR spectrum of $\alpha$-NaMnO$_2$ measured at 300 K in the applied field of 8.9 T ($\nu_0$ = 100.5255 MHz). (b) The central transition ($-1/2 \leftrightarrow 1/2$) of the same spectrum. Solid lines correspond to the fit explained in the text.

Temperature dependence of $\delta_{\rm iso}$ and $\delta_{\rm aniso}$ [Fig. 12] provides a local insight to magnetism in $\alpha$-NaMnO$_2$. Their expected scaling with magnetic susceptibility, $\delta_{\rm iso}$, $\delta_{\rm aniso} \propto \chi$, is observed at high temperatures [*cf.*

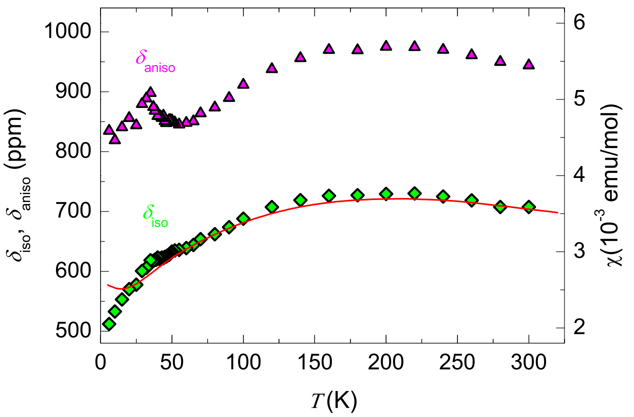

FIG. 12: The temperature dependence of the $^{23}$Na NMR line shift $\delta_{\rm iso}$ and the line width $\delta_{\rm aniso}$, compared to bulk susceptibility $\chi$ (solid line) measured at 5 T.

Fig. 3(b) of the main part]. The scaling of $\delta_{\rm iso}$ is roughly retained down to 15 K where the low-temperature upturn occurs in $\chi$ [1]. The intrinsic susceptibility $\chi_i \propto \delta_{\rm iso}$ continues decreasing down to the lowest temperatures. Much larger deviations of $\delta_{\rm aniso}$ from linearity are observed already at $\sim 60$ K and suggest a more complicated magnetic state than initially suggested [1].

Magnetization-recovery curves in spin-lattice relaxation measurements were fitted to $M_z(t) = A\left\{1-\frac{1}{5}\exp\left[-(t/T_1)^\alpha\right]-\frac{9}{5}\exp\left[-(6t/T_1)^\alpha\right]\right\}+B$, suitable for magnetic relaxation of the central line of a $I = 3/2$ nuclei [8]. We found constant stretch exponent $\alpha = 0.86(2)$ at $T > T_N$ and a significantly decreased exponent in the magnetically ordered state reaching $\alpha = 0.60(2)$ at low temperatures. The decrease of $\alpha$ below $T_N$ evidences an increased distribution of spin-lattice relaxation rates, hence a broad distribution of local environments, in line with the inhomogeneous ground state of $\alpha$-NaMnO$_2$.

## Muon Stopping Sites

It is supposed that $\mu^+$ would most likely stop at the global potential minimum of the crystal structure [9], which has been verified before on several instances [10, 11]. The calculations were carried out by applying the Quantum Espresso code [12], and by using the generalized-gradient approximation (GGA) [13] for the exchange-correlation potential. The electron-ion interactions were described with the Vanderbilt ultrasoft potentials [14]. The plane-wave cut-off parameters were set to 408 eV and 3264 eV, respectively, whereas a $4\times4\times4$ ($4\times8\times4$ for the non-spin-polarized case) mesh in the full Brillouin zone was used for the Methfessel-Paxton sampling [15] integration. Both the spin-polarized and non-polarized calculations yield the same most-probable muon site $P_1 = (0.18, 0, 0.47)$ [inset in Fig.4(c) of the main text], which is an interstitial site with site symmetry $m$ at Wyckoff position $4i$ in the monoclinic setting. Although this site is close to the Mn-layer, its nearest-neighbor site is actually O$^{2-}$ at the distance of 1.74 Å.

Calculations of the dipolar field at this site (*vide infra*) yield the magnetic field of 0.24 T that nicely corroborates the experimental $B_{\mu1} = 0.22(2)$ T. However, our *ab-initio* calculation could not find any local minimum that would correspond to $B_{\mu2} = 0.69(2)$ T. Therefore, our assignment of the second site relies on a common tendency of the muon to "bind" to O$^{2-}$ at the distance of 1.0 Å [9]. We then set the second muon stopping site to $P_2 = (0.45, 0, 0.75)$ ($4i$) on the 1.0 Å-sphere around the oxygen site, where the dipolar field matches $B_{\mu2}$ and the electrostatic potential of the unperturbed crystal structure is minimal.

The influence of a moun stopping at either $P_1$ or $P_2$ on all of the exchange constants and thus locally on the magnetic ground state is expected to be negligible. The site $P_1$ is far from any exchange path, while the site $P_2$ could possibly interfere only with the weak inter-layer path. Therefore, it is highly unlikely for the muon to cause any local inhomogeneities of the magnetic order.

## Dipolar-field calculations

Calculations of the dipolar magnetic field $\mathbf{B}_{\rm dd}(\mathbf{r}) = \frac{\mu_0}{4\pi}\sum_j\left\{\frac{\mu_j}{|\mathbf{r}-\mathbf{r}_j|^3} - \frac{3(\mathbf{r}-\mathbf{r}_j)[\mu_j\cdot(\mathbf{r}-\mathbf{r}_j)]}{|\mathbf{r}-\mathbf{r}_j|^5}\right\}$ at a given site $\mathbf{r}$ were performed by taking into account all Mn$^{3+}$ moments $\mu_j$ at sites $\mathbf{r}_j$, within a sphere centered at $\mathbf{r}$ with a radius large enough to ensure convergence. The moments were either taken polarized along the applied field in the paramagnetic state or ordered according to Ref. 1 ($\mu = 2.9\ \mu_B$ at 5 K). We find that the dipolar magnetic field at the $^{23}$Na site in the paramagnetic phase is almost axially symmetric. Its principal value amounts to $A = 0.16$ T$/\mu_B$. Taking into account the 300 K susceptibility value $\chi = 3.5\cdot10^{-3}$ emu/mol, this leads to the dipolar contribution to the anisotropic hyperfine coupling $\delta^{\rm dd}_{\rm aniso} = \frac{A\chi}{N_A} = 1000$ ppm ($N_A$ is the Avogadro number). This matches astonishingly well with the experimental $\delta_{\rm aniso} = 950$ ppm, which disclosed a negligible contribution of the transferred hyperfine interaction to $\delta_{\rm aniso}$.

When modeling the normalized local magnetic-field distributions $D(B) = \frac{1}{N_0}\frac{{\rm d}N}{{\rm d}B}$ at both muon stopping sites and at the $^{23}$Na site in the structurally inhomogeneous phase below $T_N$, we assumed that the magnetic order in the triclinic "parasitic" regions was inverted with respect to the monoclinic matrix. We calculated the magnetic field in $N_0$ points, each with a different random distribu-

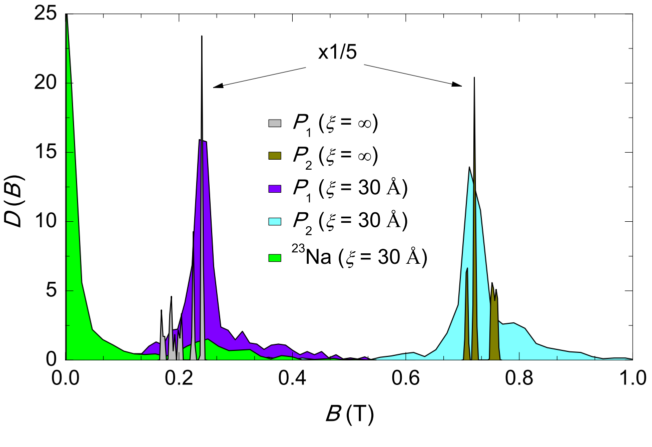

FIG. 13: Field distributions in the inhomogeneous magnetic phase of $\alpha$-NaMnO$_2$, calculated for the defect concentration $p = 0.35$ on both muon stopping sites, $P_1$ and $P_2$, and on the $^{23}$Na nuclear site. Results are shown for the one-dimensional-defect model with $\xi = \infty$ (chain-shift model) and the model of three-dimensional finite-size defects ($\xi = 30$ Å).

tion of defects with a given concentration $p$. Assuming different dimensionalities and correlation lengths of the triclinic islands, the field distribution $D(B_\mu)$ and the corresponding muon relaxation functions were calculated, $P(t) = \frac{1}{3} + \frac{2}{3}\sum_{j=1}^{2} f_j \int D(B_{\mu j})\cos(\gamma_\mu B_{\mu,j} t)\mathrm{d}B_{\mu,j}$. In Fig. 13 field distributions at the two muon stopping sites are compared for the model of one-dimensional defects with infinite $\xi$ and the model of three-dimensional defects with the size $\xi = 30$ Å, both calculated for $p = 0.35$. The former yields a few sharp peaks and the latter a broader field distribution. The two-peak field-distribution at the $^{23}$Na site obtained for the second model is also shown.

---

[*] Electronic address: andrej.zorko@ijs.si

[†] Electronic address: lappas@iesl.forth.gr

[1] M. Giot, L. C. Chapon, J. Androulakis, M. A. Green, P. G. Radaelli, and A. Lappas, Phys. Rev. Lett. **99**, 247211 (2007).

[2] A. Zorko, S. El Shawish, D. Arčon, Z. Jagličić, A. Lappas, H. van Tol, and L. C. Brunel, Phys. Rev. B **77**, 024412 (2008).

[3] C. Stock, L. C. Chapon, O. Adamopoulos, A. Lappas, M. Giot, J. W. Taylor, M. A. Green, C. M. Brown, and P. G. Radaelli, Phys. Rev. Lett. **103**, 077202 (2009).

[4] P. W. Stephens, J. Appl. Cryst. **32**, 281 (1999).

[5] C. Vecchini, M. Poienar, F. Damay, O. Adamopoulos, A. Daoud-Aladine, A. Lappas, J. M. Perez-Mato, L. C. Chapon, and C. Martin, Phys. Rev. B **82**, 094404 (2010).

[6] M. Poienar, C. Vecchini, G. André, A. Daoud-Aladine, I. Margiolaki, A. Maignan, A. Lappas, L. Chapon, M. Hervieu, F. Damay, and C. Martin, Chem. Mater. **23**, 85 (2011).

[7] E. Dagotto, Science **309**, 257 (2005).

[8] A. Suter, M. Mali, J. Roos, and D. Brinkmann, J. Phys.: Condens. Matter **10**, 5977 (1998).

[9] A. Yaouanc and P. Dalmas de Réotier *Muon Spin Rotation, Relaxation and Resonance* (Oxford University Press, Oxford, 2011).

[10] H. Luetkens, M. Stingaciu, Yu. G. Pashkevich, K. Conder, E. Pomjakushina, A. A. Gusev, K. V. Lamonova, P. Lemmens, and H.-H. Klauss, Phys. Rev. Lett. **101**, 017601 (2008).

[11] M. Pregelj, A. Zorko, O. Zaharko, D. Arčon, M. Komelj, A. D. Hillier, and H. Berger, Phys. Rev. Lett. **109**, (2012).

[12] P. Gianozzi *et al.*, J. Phys.: Condens. Matter **21**, 395502 (2009).

[13] J. Perdew, K. Burke, and M. Ernzerhof, Phys. Rev. Lett. **77**, 3865 (1996).

[14] D. Vanderbilt, Phys. Rev. B **41**, R7892 (1990).

[15] M. Methfessel and A. T. Paxton, Phys. Rev. B **40**, 3616 (1989).